ACS OMEGA

http://pubs.acs.org/journal/acsodf

Article

# Importance of Process Variables and Their Optimization for Oxidative Coupling of Methane (OCM)

Sultan Alturkistani,* Haoyi Wang, Ribhu Gautam,* and S. Mani Sarathy

Cite This: *ACS Omega* 2023, 8, 21223−21236

Read Online

ACCESS | Metrics & More | Article Recommendations

**ABSTRACT:** Oxidative coupling of methane (OCM) is a promising process for converting natural gas into high-value chemicals such as ethane and ethylene. The process, however, requires important improvements for commercialization. The foremost is increasing the process selectivity to $C_2$ ($C_2H_4$ + $C_2H_6$) at moderate to high levels of methane conversion. These developments are often addressed at the catalyst level. However, optimization of process conditions can lead to very important improvements. In this study, a high-throughput screening (HTS) instrument was utilized for $La_2O_3/CeO_2$ (3.3 mol % Ce) to generate a parametric data set within the temperature range of 600−800 °C, $CH_4/O_2$ ratio between 3 and 13, pressure between 1 and 10 bar, and catalyst loading between 5 and 20 mg leading to space-time between 40 and 172 s. Statistical design of experiments (DoE) was applied to gain insights into the effect of operating parameters and to determine the optimal operating conditions for maximum production of ethane and ethylene. Rate-of-production analysis was used to shed light on the elementary reactions involved in different operating conditions. The data obtained from HTS experiments established quadratic equations relating the studied process variables and output responses. The quadratic equations can be used to predict and optimize the OCM process. The results demonstrated that the $CH_4/O_2$ ratio and operating temperatures are key for controlling the process performance. Operating at higher temperatures with high $CH_4/O_2$ ratios increased the selectivity to $C_2$ and minimized $CO_x$ (CO + $CO_2$) at moderate conversion levels. In addition to process optimization, DoE results also allowed the flexibility of manipulating the performance of OCM reaction products. A $C_2$ selectivity of 61% and a methane conversion of 18% were found to be optimum at 800 °C, a $CH_4/O_2$ ratio of 7, and a pressure of 1 bar.

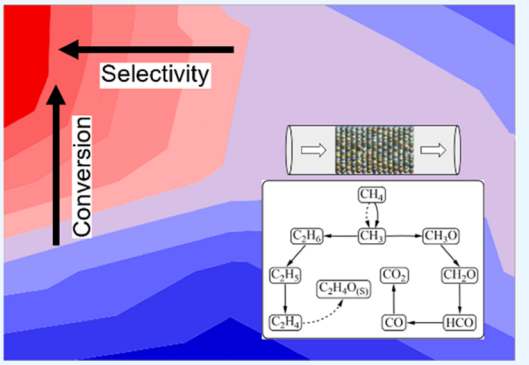


## 1. INTRODUCTION

Because of its low cost and availability, natural gas is an attractive feedstock in today's energy market. At the same time, its increasing availability escalates interest in conversion to more valuable commodity chemicals and fuels.[1] The concept of methane conversion to higher-value chemicals is not novel; researchers have investigated different processes for decades.[1,2] Despite several attempts, the oxidative coupling of methane (OCM) to $C_2$ hydrocarbons appears promising. Keller and Bhasin[3] pioneered the process in the early 1980s by activating methane molecules without a catalyst using oxygen at temperatures above 800 °C. The conversion of methane without oxygen is highly endothermic and is limited by thermodynamic boundaries.[4] Catalysts were proposed later to decrease the activation energy and shift the reaction pathways of the OCM toward the desired products. The reaction representing the process, $2CH_4 + O_2 \leftrightarrow C_2H_4 + 2H_2O$, occurs via a series of homogeneous and heterogeneous reaction steps.[5−7] The $C_2$ yield achieved for the OCM is still below 30%, which has been a barrier against commercialization.[8] To achieve commercialization, a sustainable process with a $C_2$ single-pass yield of more than 25−30% is required.[9,10] The $C_2$ yield, however, is restricted at elevated temperatures in the presence of oxygen by the complete oxidation reactions to $CO_x$.[11,12] Thus, considerable effort has been dedicated to developing an active and selective catalyst for the OCM.

A range of catalysts has been studied to overcome the conversion−selectivity trade-off resulting from the low reactivity of methane toward $C_2$ products.[11,13−22] A Mn/$Na_2WO_4/SiO_2$ material was identified as the first OCM catalyst by Fang et al.[16] Doping Mn/$Na_2WO_4/SiO_2$ with alkali chlorides (LiCl, NaCl, KCl, CsCl) increased the ethylene yield.[17] Mn/$Na_2WO_4/SiO_2$ can also be operated at high temperatures, up to 900 °C, with decent stability and performance.[16] Li/MgO catalysts are another potential material developed by Ito et al.[23] and were one of the most

Received: April 7, 2023
Accepted: May 18, 2023
Published: May 30, 2023

extensively studied catalysts for the OCM. Li/MgO showed a high catalytic activity and exhibited a moderate $C_2$ yield (≤20%), but they suffered from poor stability, originating from continuous Li+ loss and morphology changes above 800 °C.[4,24] Researchers have been motivated to investigate other groups of catalysts offering chemical stability and structural integrity under process-designed operating conditions. Apart from experimental approaches, statistical methods were also utilized to search for better catalysts. Zavyalova et al.[25] statistically analyzed a database of 1870 data sets for OCM catalysts to determine the optimal catalyst composition. They found that La-based catalysts exhibited the highest $C_2$ selectivity. Siluria Technologies has claimed to have developed the first OCM commercial process and has patented a series of nanowire catalysts containing two different lanthanide-group metals, such as La−Pr, La−Zr, and La−Ce.[2,26] Doping $La_2O_3$ with metals such as Sr, Mg, Ca, and Ce enhanced the catalytic activity and promoted higher $C_2$ selectivity.[27] $La_2O_3$ doped with cerium in a packed bed reactor increased the $C_2$ selectivity and inhibited coke formation with a $C_2$ yield of 18%.[28]

Research on the OCM process is generally focused on catalysis development, although several other factors are involved in the process improvement. Since the OCM process is currently under research and development, experimental conditions in previous studies were inconsistent across similar or different reactor configurations. As La-based catalysts have been developed at a commercial scale for the OCM process, investigating such catalysts is worthwhile using experiments and statistical tools. $La_2O_3$-based catalysts, for example, were investigated in the temperature range of 350−850 °C and $CH_4/O_2$ ratio between 2 and 16.[29−32] Due to the wide range of parameters examined, a number of research articles were published between 2006 and 2021 on optimizing the OCM process variables.[33−38] These research articles have mainly focused on applying statistical methods to the experimental data in a wide range of process conditions without discussing the elementary reactions involved. However, using analysis of variance (ANOVA) and high-throughput screening (HTS) with the incorporation of elementary reactions at the same time can develop a better understanding for optimization of the process. This study performs a more robust optimization of a $La_2O_3/CeO_2$ catalyst using experimental data obtained from a high-throughput screening (HTS) instrument and sheds light on the elementary reactions involved. The main reaction pathways were investigated using a rate-of-production (ROP) analysis at different operating conditions. The ROP and experimental data over a wide range of operating conditions are provided in our previous study.[39] The gas-phase reactions were taken from AramcoMech3.0,[40] while the surface reactions were obtained from Karakaya et al.[11] Experimental results were statistically analyzed through the DoE method using JMP, Version 16. The derived statistical models were evaluated based on the analysis of variance (ANOVA) at a 5% level of significance.

## 2. EXPERIMENTS AND METHODOLOGY

**2.1. Catalyst Preparation.** The $La_2O_3/CeO_2$ catalyst used in this study was prepared through the citric acid sol−gel method.[41−43] $La(NO_3)_3{\cdot}6H_2O$ (99.99%) and $Ce(NO_3)_3{\cdot}6H_2O$ (99.99%) were used as precursors to synthesize the catalyst. The doping percent for $Ce(NO_3)_3{\cdot}6H_2O$ was chosen to be five mol % of $La(NO_3)_3{\cdot}6H_2O$. The precursor materials were dissolved in distilled water and mixed with citric acid that has the same mol % as $La(NO_3)_3{\cdot}6H_2O$. The mixture was stirred with a magnetic stir bar for 20 min to achieve a homogeneous solution. Under continuous stirring, the solution was dried in an oil bath at 85 °C to evaporate the excess water and form a viscous gel. The gel obtained was dried at 110 °C for 8 h in a ventilated oven. The dried material was calcined at 800 °C for 5 h, with a temperature increment of 2 °C/min. The resulting material was crushed, pelletized, and sieved to a particle size of 0.15−0.25 mm (60−100 mesh) to achieve the desired particle size and prevent pressure drop in the reactor.

**2.2. Catalyst Characterization.** The $La_2O_3/CeO_2$ catalyst was analyzed to determine its surface area, metal composition, and crystallinity. The specific surface area was calculated through nitrogen adsorption and desorption isotherms using the Brunauer−Emmett−Teller (BET) method. The isotherms were recorded using a Micromeritics ASAP 2420 Surface Area and Porosimetry System at 77K. To remove trapped impurities, the catalyst was first degassed at 90 °C for 240 min and then at 350 °C for 720 min under vacuum condition. The $P/P_0$ range for BET analysis was $0.067 < P/P_0 < 0.249$. A type IV adsorption isotherm was obtained for the fresh catalyst with a BET surface area of 12 $m^2/g$, which is comparable to previous studies.[28]

The actual doping percentage of Ce metal within the catalyst material was determined via inductively coupled plasma (ICP) analysis using an ICP-OES Varian 72 ES system. The catalyst material was pretreated by dissolving in HCl and $HNO_3$ at 120 °C for 40 min using an UltraWAVE digestion system. The composition of Ce was found to be 3.3% in the catalyst. The reduction in metal content from 5 to 3.3% occurred during the calcination process. During calcination, the material oxidizes in the presence of oxygen at high temperatures, in addition to the removal of volatiles.

The crystallinity of the material was determined for fresh and spent catalysts through X-ray diffraction (XRD). The spectra were collected in the 2$\theta$ range of 0−80° with a step size of 0.02° using a Bruker D8 Advanced A25 diffractometer equipped with Cu K$\alpha$ radiation. The crystalline phases were identified by comparison with the Inorganic Crystal Structure Database (ICSD). The XRD patterns for the fresh and spent catalysts are shown in Figure 1. The sharp peaks indicated that

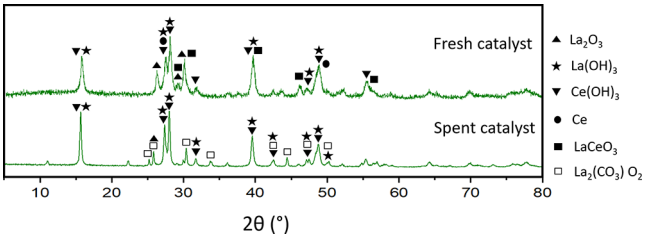


**Figure 1.** XRD patterns for fresh and spent catalysts.

the material was well crystallized. A hexagonal structure was detected for $La_2O_3/CeO_2$, and peaks were identified for $La_2O_3$,[44] $La(OH)_3$,[45,46] $Ce(OH)_3$,[47] Ce,[48] $LaCeO_3$,[49] and $La_2(CO_3)O_2$.[50] A change of $La_2O_3$ to $La_2O_2CO_3$ was observed between fresh and spent catalysts (Figure 1). Above 650 °C, $La_2O_3$ reacted with $CO_2$ produced in the process to form a dioxymonocarbonate ($La_2O_2CO_3$) structure through $La_2O_3 + CO_2 \rightarrow La_2O_2CO_3$. The dioxymonocarbonate is another active OCM catalyst.[20,51]



https://doi.org/10.1021/acsomega.3c02350
ACS Omega 2023, 8, 21223−21236

**2.3. Experimental Setup.** This study conducted experiments on a Flowrence HTS unit from Avantium equipped with 16 parallel fixed-bed reactors. The reactors were made of quartz and had dimensions of 2 mm (i.d.) × 3 mm (o.d.) × 30 cm (length). The 16 reactors were kept in four electric furnaces for temperature control. Due to the high operating temperature, quartz reactors were used to maintain their inertness at elevated temperatures. To reduce the radial temperature gradients, silicon dioxide ($SiO_2$) was added to the catalyst bed with a dilution ratio of 1/10. The $SiO_2$ particles were of the same size as the catalyst particles to ensure a uniform gas velocity distribution. The reactants and products were identified using an online Varian 490-Micro GC gas chromatograph (GC) equipped with two channels comprising different columns for the detection of different components via thermal conductivity detectors. Methane, carbon monoxide, oxygen, hydrogen, helium, and nitrogen were separated and identified through the first channel, while the second channel detects carbon dioxide and $C_2$−$C_4$ hydrocarbons. The details of the experimental setup can be obtained from a previous study.[39] The investigated process variables for DoE were temperature, $CH_4/O_2$ ratio, pressure, and catalyst loading. The range of operating parameters and DoE factor codes are listed in Table 1. The ranges were determined based on the results of the previous studies and screening experiments.[29−32] The inlet methane concentration was 0.7 mol % at 298 K with a total flow rate of 137 mL/min. The catalyst loading reflects space-time between 40 and 172 s. The catalyst bed lengths with $SiO_2$ dilution for 5, 10, and 20 mg loading were 1.5, 3, and 6 cm, respectively. In order to minimize uncontrolled effects, the sequence of experiments was randomized. The explored responses were methane conversion and the selectivities of ethylene, ethane, carbon monoxide, carbon dioxide, and the yield of ethylene and ethane. A database of over 150 data points comprising conversion and product selectivities was generated for the DoE optimization.

**Table 1. Range of Operating Parameters for DoE**

| factors | factor code | range of factors change |
|---|---|---|
| $CH_4/O_2$ | *A* | 3−5−7−9−11−13 |
| temperature (°C) | *B* | 600−650−700−750−800 |
| catalyst loading (mg) | *C* | 5−10−20 |
| pressure (bar) | *D* | 1−5−10 |

**2.4. Experimental Design and Method of Analysis.** DoE is a scientific method for designing and analyzing a series of experiments to determine the most precise relationship between process variables and exit gas composition.[52] DoE was developed to consider all possible interactions between variables compared to the traditional "one-variable-at-a-time" approach. DoE manipulates each process variable individually to identify invisible links among them, including main, two-way, and three-way interactions. The experimental space in the "one-variable-at-a-time" method considers only the main effect and may not capture hidden interactions between variables, as discussed later. From different DoE designs, the full factorial design (FFD) was chosen based on its comparable accuracy. FFD studies all of the possible combinations of input variables and their respective range of values.[52] FFD is a set of mathematical and statistical algorithms built for analyzing optimization problems. The effects of all process variables were investigated using a stepwise linear model with a backward direction and a minimum Bayesian information criterion (BIC) stopping rule. The ANOVA method was applied to identify the power factors by calculating the *P*-value, *F* ratio, and *R* square ($R^2$).

Since the DoE parameters have been explained previously,[52] only a summary is provided here. The *P*-value represents a probability that ranges between zero and one and is used to evaluate the significance of each variable. Variables with a *P*-value less than 0.05 (level of significance) have a high effect.[52] In optimization research using DoE and ANOVA, the level of significance is typically set at 0.05, as per standard practice.[33,34]

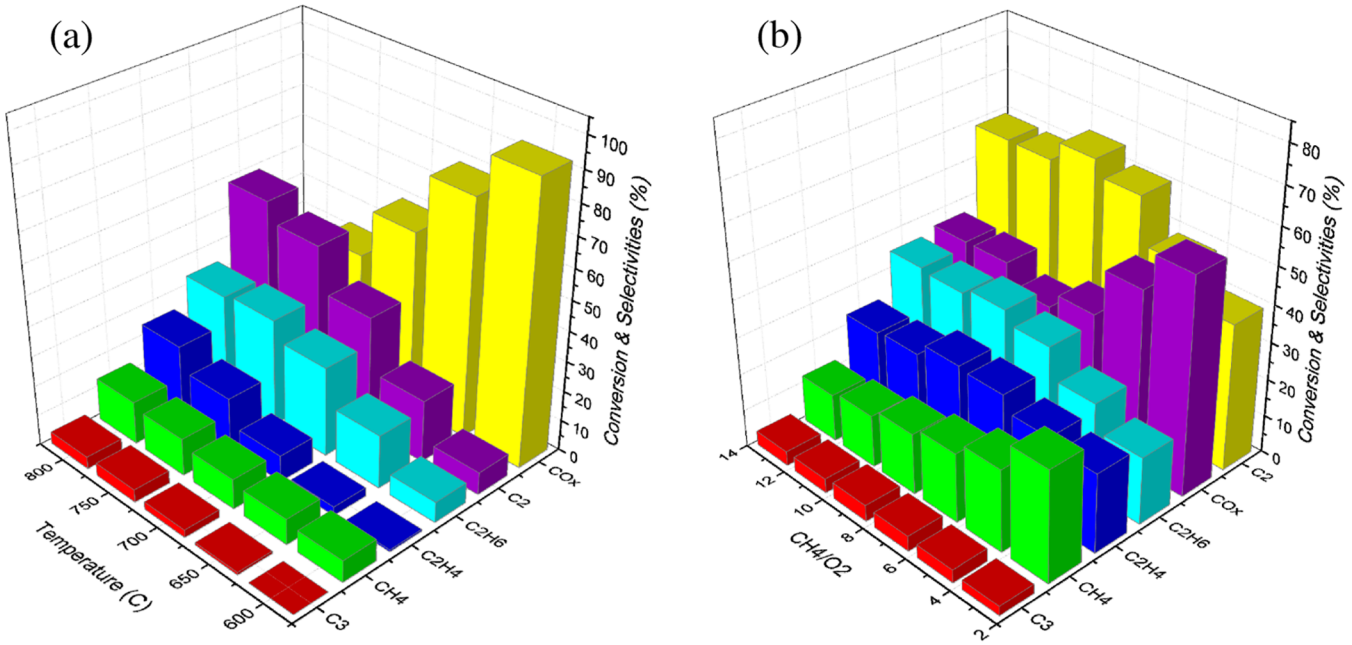


**Figure 2.** Effect of (a) temperature at $CH_4/O_2$ = 11 and (b) $O_2$ concentration at 800 °C. Catalyst diluted with $SiO_2$. 20 mg of catalyst. The experimental error is within 5%.



https://doi.org/10.1021/acsomega.3c02350
ACS Omega 2023, 8, 21223−21236

The $F$ ratio measures the variance of the data around its mean. Consequently, the smaller the $P$-value and the higher the $F$ ratio, the more significant the variable. The mean square represents an estimate of population variance, while the sum of squares measures the variation of all observations from their mean.[52] $R^2$ describes the difference between the DoE-predicted and the observed experimental values. As a practical rule of thumb, $R^2$ should be greater than 0.75 to ensure a reasonable prediction.[52] The calculated values of the $F$ ratio, $P$-value, and $R^2$ are in the corresponding ANOVA tables and parity plots. The results of the HTS experiments established a functional relationship between input process variables and output responses. Based on the experimental data, the software chose the quadratic equation among several functional models, such as linear, polynomial (3rd degree and beyond), etc., to describe the relationship between input variables and responses. As a result, optimization can be performed either experimentally or analytically using quadratic equations. Each quadratic equation partitions into linear, quadratic, and interaction $\beta$ coefficients as $Y = \beta_o + \beta_1 A + \beta_2 B + \beta_3 C + \beta_{12} A*B + \beta_{13} A*C + \beta_{23} B*C + \beta_{11} A^2 + \beta_{22} B^2 + \beta_{33} C^2$, where $Y$ is the predicted response and A−C are the coded forms of process variables. $\beta_o$ is the offset term, and $\beta_{1-3}$ are the linear coefficients. $\beta_{11}$, $\beta_{22}$, and $\beta_{33}$ are the squared coefficients, and $\beta_{12}$, $\beta_{13}$, and $\beta_{23}$ are the interaction coefficients. The cutoff value of the $\beta$ coefficients is set at 0.05, which represents the level of significance. Any $\beta$ coefficients that have a $P$-value less than 0.05 were considered significant and included in the quadratic formulae. Not all $\beta$ coefficients in the derived quadratic formula met the level of significance criteria and thus were eliminated from the formula, retaining only the significant terms.

## 3. RESULTS AND DISCUSSION

The results of the DoE analysis demonstrated the influence of operating parameters and the ability to control the process performance. Prior to optimization, the input factors were screened to determine the appropriate optimization plan for the DoE analysis. First, the temperature was varied at a selected $CH_4/O_2$ ratio of 11 based on previous findings.[39] The results showed that temperature significantly impacted the process (Figure 2a). Consequently, a range between a low conversion level at 600 °C to the maxima temperature that can be operated in the HTS unit, 800 °C, was included in the DoE analysis. Subsequently, at the best-observed temperature of 800 °C, the $CH_4/O_2$ ratio, pressure, and catalyst loading were varied to assess their respective effects on process performance. The results showed that an increase in pressure had a negative impact on methane conversion, and it promoted undesirable total oxidation products, leading to an increase in the process cost. Since the pressure had a negative effect and for experimental safety, the effect of pressure was investigated for $CH_4/O_2$ ratios of 7 and 9. An increase in the $CH_4/O_2$ ratio at 800 °C decreased conversion and increased $C_2$ selectivity notably (Figure 2b). These results suggest that the effect of the $CH_4/O_2$ ratio should be investigated at a wide range across other operating conditions. Catalyst loading exhibited a weaker impact within the investigated range of operating conditions. A detailed discussion of the results is presented in the subsequent sections.

### 3.1. Methane Conversion.

The quadratic formula for methane conversion is given in eq 1. The calculated value of $R^2$ is 0.9. Thus, the derived equation satisfactorily predicts the conversion. Observed deviations could be attributed to possible GC errors that arise during experimental measurements. The parity plot depicted in Figure 3 portrays the

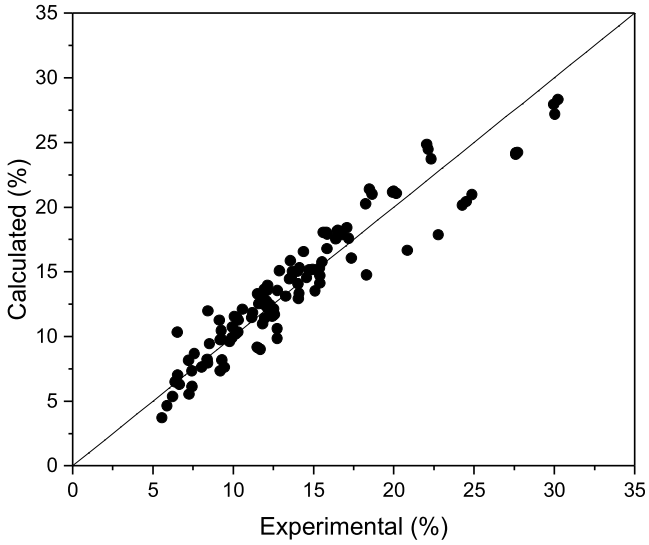


**Figure 3.** Methane conversion parity plot for the experimental and predicted values.

variation between predicted and experimentally measured values of methane conversion. The evenly distributed data points along the plot diagonal signify a symmetrical pattern, reflecting the analytical accuracy of the prediction.

$$\begin{aligned}\text{methane conversion (\%)} &= 13.3 - 6.4\frac{A-8}{5} + 3.32\frac{B-700}{100} + 0.41\frac{C-12.5}{7.5} \\ &\quad - 0.87\frac{D-5.5}{4.5} - 2.27\frac{A-8}{5}\frac{B-700}{100} \\ &\quad - 0.98\frac{C-12.5}{7.5}\frac{B-700}{100} - 1.61\frac{B-700}{100}\frac{D-5.5}{4.5}\end{aligned} \quad (1)$$

A comprehensive summary of the ROP analysis results is provided in Figure 4, outlining the main reaction pathways, product distributions, and contribution of homogeneous and heterogeneous reactions. Surface reactions contributed primarily to methane activation, while gas-phase reactions determined the distribution of end products. The effect of the $CH_4/O_2$ ratio on methane conversion was found to be the most

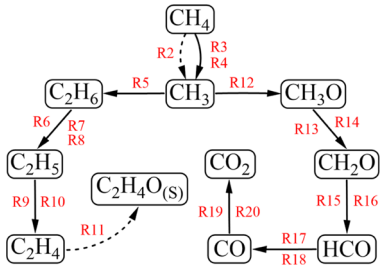


**Figure 4.** General reaction pathways representing the OCM chemistry. Adapted with permission from Alturkistani et al.[39] Copyright 2022 Society of Petroleum Engineers (SPE). Gas-phase reactions are shown as solid arrows, and surface reactions are shown as dashed arrows. Reactions are presented in Table 2.


https://doi.org/10.1021/acsomega.3c02350
ACS Omega 2023, 8, 21223−21236

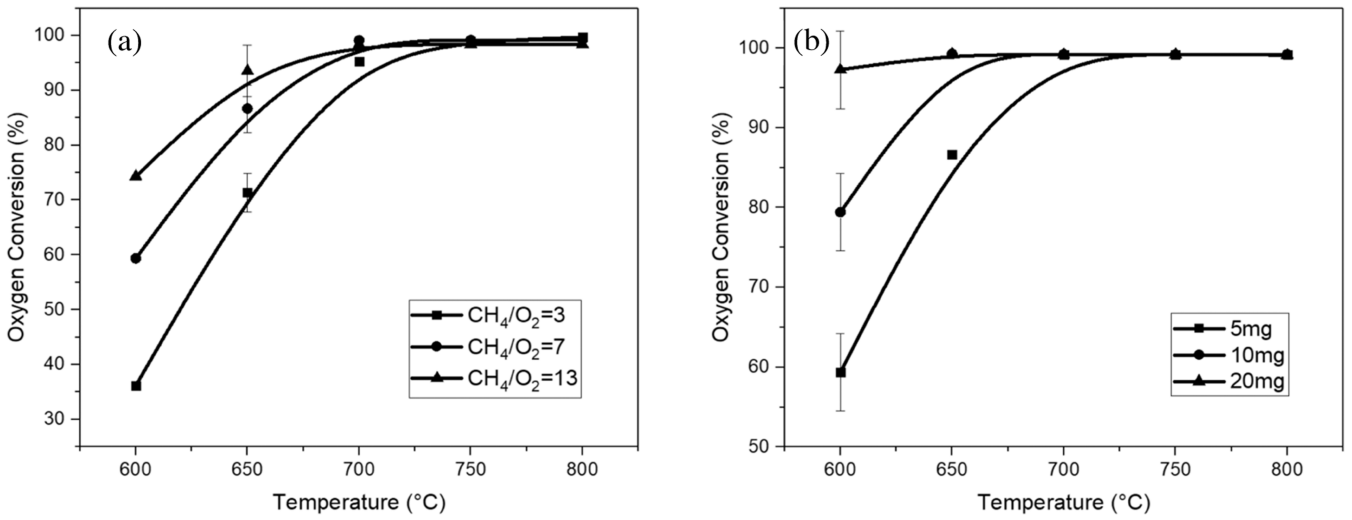


**Figure 5.** Oxygen conversion for (a) 5 mg catalyst loading, (b) $CH_4/O_2$ = 7. Catalyst diluted with $SiO_2$, 70.7 kPa $CH_4$, 101 kPa total pressure, $N_2$ as balance, and inlet volumetric flow rate 137 $cm^3$/min at 25 °C. The experimental error is within 5%. The lines represent B-spline fitting to the experimental data points.

**Table 2. Important Gas-Phase and Surface Reactions for the OCM[a]**

| # | reaction | classification of reaction | # | reaction | classification of reaction |
|---|---|---|---|---|---|
| 1 | $O_2 + 2La(s) \rightarrow 2O(s)$ (1) | surface phase | 11 | $C_2H_4 + O(s) \rightarrow C_2H_4O(s)$ (11) | surface phase |
| 2 | $CH_4 + O(s) \rightarrow CH_3 + OH(s)$ (2) | surface phase | 12 | $CH_3 + HO_2 = CH_3O + OH$ (12) | gas phase |
| 3 | $CH_4 + H = CH_3 + H_2$ (3) | gas phase | 13 | $CH_3O(+M) = CH_2O + H(+M)$ (13) | gas phase |
| 4 | $CH_4 + OH = CH_3 + H_2O$ (4) | gas phase | 14 | $CH_3O + O_2 = CH_2O + HO_2$ (14) | gas phase |
| 5 | $2CH_3(+M) = C_2H_6(+M)$ (5) | gas phase | 15 | $CH_2O + H = HCO + H_2$ (15) | gas phase |
| 6 | $C_2H_6 + H = C_2H_5 + H_2$ (6) | gas phase | 16 | $CH_2O + CH_3 = HCO + CH_4$ (16) | gas phase |
| 7 | $C_2H_6 + CH_3 = C_2H_5 + CH_4$ (7) | gas phase | 17 | $HCO + M = H + CO + M$ (17) | gas phase |
| 8 | $C_2H_6 + OH = C_2H_5 + H_2O$ (8) | gas phase | 18 | $HCO + O_2 = CO + HO_2$ (18) | gas phase |
| 9 | $C_2H_5(+M) = C_2H_4 + H(+M)$ (9) | gas phase | 19 | $CO + OH = CO_2 + H$ (19) | gas phase |
| 10 | $C_2H_5 + O_2 = C_2H_4 + HO_2$ (10) | gas phase | 20 | $CO + HO_2 = CO_2 + OH$ (20) | gas phase |

[a]Adapted from Karakaya et al.[11] Copyright 2017 John Wiley and Sons. Adapted from Zhou et al.[40] Copyright Elsevier 2018.

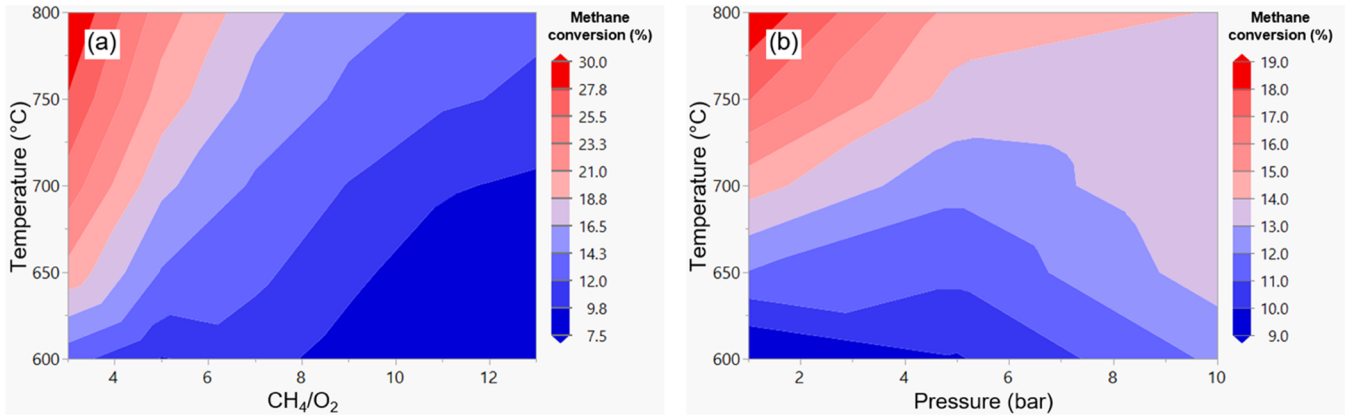


**Figure 6.** Methane conversion contour plots for (a) $CH_4/O_2$ versus temperature and (b) pressure versus temperature. Plots averaged all results based on the DoE calculation procedure.

significant, with the primary (linear) and interaction (quadratic) effects being confirmed by a *P*-value of less than 0.0001, which is below the threshold level of significance (Table 3). The oxygen availability represented by the $CH_4/O_2$ ratio served as the rate-determining step that initiated the reaction chain. This is demonstrated in the literature as well.[11] Figure 5 shows that the fed oxygen was fully consumed in all of the conducted experiments at 750 and 800 °C. The oxygen conversion reached 100% under various $CH_4/O_2$ ratios (Figure 5a) and different catalyst loadings (Figure 5b). The


https://doi.org/10.1021/acsomega.3c02350
ACS Omega 2023, 8, 21223−21236

Table 3. ANOVA Table of Methane Conversion

| predictor | factor code | degree of freedom | sum of squares | $F$ ratio | prob > $F$ |
|---|---|---|---|---|---|
| $CH_4/O_2$ | $A$ | 1 | 1753.93 | 495.4 | <.0001 |
| temperature | $B$ | 1 | 199.46 | 56.34 | <.0001 |
| catalyst weight | $C$ | 1 | 11.12 | 3.14 | 0.0793 |
| pressure | $D$ | 1 | 24.08 | 6.8 | 0.0105 |
| $CH_4/O_2$*temperature | $A$*$B$ | 1 | 110 | 31.07 | <.0001 |
| temperature*catalyst weight | $B$*$C$ | 1 | 31.12 | 8.79 | 0.0038 |
| temperature*pressure | $B$*$D$ | 1 | 41.37 | 11.69 | 0.0009 |
| source | degree of freedom | sum of squares | $F$ ratio | mean square | |
| model | 7 | 3094.15 | 124.85 | 442.02 | |
| error | 102 | 361.12 | prob > $F$ | 3.54 | |
| C. total | 109 | 3455.27 | <.0001 | | |

OCM was initiated on the catalyst surface through the dissociative chemisorption of oxygen (reaction R1), followed by methane adsorption onto the same surface. It can be noted that the reaction numbers throughout the manuscript are invoked from Table 2. This adsorbed methane subsequently reacted with the surface oxygen to form a methyl radical ($CH_3$*) (reaction R2). The experimental results indicated that the initiation reaction was facilitated by an increase in oxygen concentrations, which resulted in a substantial increase in methane conversion from 12% to more than 30% at 800 °C (Figure 6a). It is worth noting that the DoE figures in this paper present an average of all of the experimental results based on the DoE calculation procedure.

Apart from the $CH_4/O_2$ ratio, temperature was also found to significantly affect the methane conversion, with a $P$-value less than 5%, as shown in Table 3. Methane is a stable molecule characterized by a regular tetrahedron structure, exhibiting a perfectly symmetric zero dipole moment with a C−H bond energy of around 439 kJ/mol.[2] To break this stable molecule, high temperatures (e.g., $T$ > 700 °C) are needed, in addition to a selective catalyst to accelerate the conversion process.[2] Hence, both the linear and quadratic effects of temperature and catalyst loading were important for methane conversion (Table 3). The increase in catalyst loading provided additional coupling and oxygenated sites for oxygen chemisorption, while the high temperatures facilitated the C−H bond breaking. The homogeneous reactions R3 and R4 in Figure 4 were also found to participate in the conversion of methane. These reactions are endothermic in nature and necessitate the provision of thermal energy in the form of temperature. Increasing the temperature from 600 to 800°C increased the conversion from 11 to ∼30% at a $CH_4/O_2$ ratio of 3 (Figure 6a). To summarize, it was found that the conversion rate decreased with an increase in the $CH_4/O_2$ ratio and increased with higher temperatures within the investigated range of conditions. The pressure effect in Figure 6b shows that the increase in pressure from 1 to 10 bar decreased methane conversion by ∼30% at 800 °C. These observations aligned with the previous literature.[33−37,53] The maximum observed conversion was 30.2% at 800 °C, a $CH_4/O_2$ ratio of 3, and a pressure of 1 bar.

**3.2. Ethane and Ethylene ($C_2$) Selectivity.** The quadratic formulae for ethane, ethylene, and $C_2$ selectivities are shown in eqs 2−4 with corresponding $R^2$ values of 0.9, 0.92, and 0.94, respectively. The obtained $R^2$ values demonstrate the accuracy of the equations in predicting the $C_2$ products. The $C_2$ products parity plots are shown in Figure 7 and exhibit a symmetrical distribution of the data points around the diagonal.

$$\text{ethane selectivity (\%)} = 13.92 + 8.47\frac{A-8}{5} + 7.01\frac{B-700}{100} - 5.37\frac{D-5.5}{4.5} + 2.27\frac{A-8}{5}\frac{B-700}{100} - 7.45\frac{B-700}{100}\frac{D-5.5}{4.5} \quad (2)$$

$$\text{ethylene selectivity (\%)} = 8.39 + 1.37\frac{A-8}{5} + 8.59\frac{B-700}{100} - 1.7\frac{D-5.5}{4.5} - 4.23\frac{B-700}{100}\frac{D-5.5}{4.5} \quad (3)$$

$$C_2\ \text{selectivity (\%)} = 22.31 + 9.84\frac{A-8}{5} + 15.6\frac{B-700}{100} - 7.07\frac{D-5.5}{4.5} + 2.68\frac{A-8}{5}\frac{B-700}{100} - 11.67\frac{B-700}{100}\frac{D-5.5}{4.5} \quad (4)$$

Ethane was mainly controlled by the $CH_4/O_2$ ratio with a $P$-value less than 5%, as shown in Table 4. As previously stated, the presence of oxygen contributed to the formation of methyl radicals, whereas the combination of two methyl radicals yielded ethane.[16,21,54] Thermodynamically, the formation of ethane requires less activation energy than ethylene.[11] According to the GC results, the obtained selectivities mainly resulted from $C_2$ and $CO_x$, with a minor contribution from $C_3$ hydrocarbons, which was less than 5%, given that the end products were primarily formed through gas-phase reactions. Gas-phase reactions of $C_1$−$C_4$ hydrocarbons have been extensively studied and comprehended at the fundamental level.[10,55,56] The ROP analysis was conducted using the AramcoMech3.0 gas-phase kinetic model,[40] which provides detailed information on the combustion kinetics of $C_0$−$C_4$, thermochemical properties and transport properties of different fuels, including methane. Figure 4 shows that methyl radicals undergo two main homogeneous conversion pathways. The first pathway shows the conversion of methyl radicals to $CH_3O$ via reaction R12, while the second shows the conversion of methyl radicals to $C_2H_6$ via reaction R5. The conversion of methyl radicals via reaction R5 does not require oxygen, unlike reaction R12. Thus, excess oxygen was found to have a limited impact on $C_2$ formation from methyl radicals



https://doi.org/10.1021/acsomega.3c02350
ACS Omega 2023, 8, 21223−21236

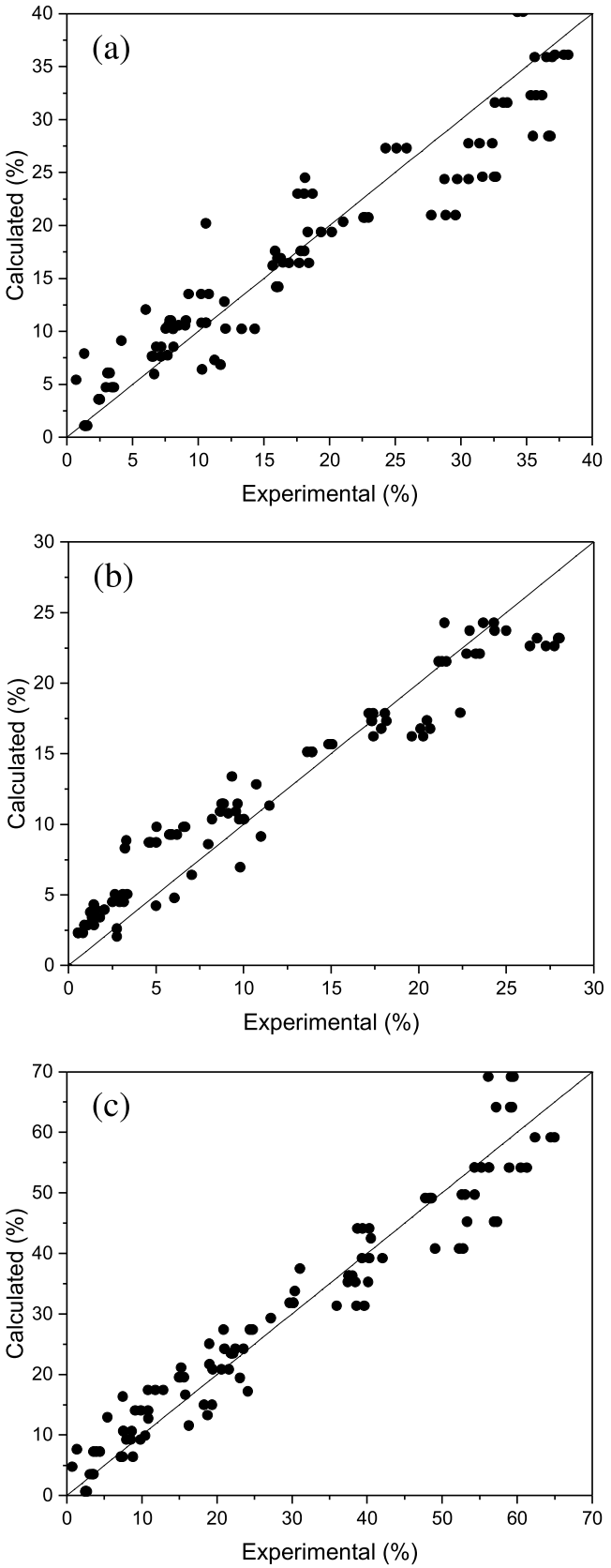


**Figure 7.** Parity plots for the experimental and DoE-predicted values for the selectivities of (a) ethane, (b) ethylene, and (c) $C_2$.

and instead favored the formation of undesired products.[33,36] Increasing the $CH_4/O_2$ ratio from 3 to 13 at 800 °C increased ethane selectivity from 16 to 36%, as shown in Figure 8a.

The DoE results showed that the temperature exhibited the second significant impact on ethane selectivity (Table 4). The variables with the highest effect were linear, followed by the quadratic terms, as determined by the ANOVA table. The activation energy of reaction R5 is positive, while the activation energy of reaction R12 is negative.[40] Thus, the process increased the selectivity of $C_2$ over $CO_x$ with the increase in temperature. Increasing the temperature from 600 to 750 °C increased the ethane selectivity from 3 to 36% at a $CH_4/O_2$ ratio of 13 (Figure 8a). The selectivity toward ethane increased until 750 °C, beyond which it slightly decreased at $CH_4/O_2$ ratios greater than 10. This behavior was attributed to the increased dehydrogenation rate of ethane to ethyl radicals.[57] The highest ethane selectivity of 38.2% was achieved at a $CH_4/O_2$ ratio of 13, temperature of 750 °C, and pressure of 1 bar. The effect of pressure on ethane selectivity is demonstrated in Figure 8b. As previously stated, analyzing the pressure effect through the "one-variable-at-a-time" approach may be misleading. The ethane selectivity showed a minor dependence on pressure at 600 °C, which decreased from ∼8 to ∼4.5%. Conversely, at 800 °C, the ethane selectivity exhibited a more pronounced pressure dependence, decreasing from around ∼30 to ∼7%. The DoE plots provide a more comprehensive representation of the impact of the process variable.

The ethylene selectivity was primarily influenced by temperature, with minimal impact from the $CH_4/O_2$ ratio (Table 5). Ethylene was formed mainly through the dehydrogenation of ethane to an ethyl radical ($C_2H_5$*) via reactions R6−R8, followed by subsequent dehydrogenation steps via reaction R9 at 800 °C and reaction R10 at 600 °C.[39] It is noteworthy that different reaction pathways were observed due to the higher activation energy and temperature requirements of reaction R9 compared to reaction R8. With the temperature increased from 650 to 800 °C, the selectivity of ethylene increased from 2.5% to more than 25% at a $CH_4/O_2$ ratio of 11, as depicted in Figure 10a. For assessing the effect of the $CH_4/O_2$ ratio on the $C_2H_4/C_2H_6$ ratio at different temperatures, $C_2H_4/C_2H_6$ at 750 °C was divided by $C_2H_4/C_2H_6$ at 650 °C. The increase in temperature resulted in a noticeable increase in the $C_2H_4/C_2H_6$ ratio of around 2.9 at a $CH_4/O_2$ ratio of 13 and above 3.7 at a $CH_4/O_2$ ratio of 3, as shown in Figure 9. These observations are consistent with a previous literature.[32,58] This may be attributed to the increase in the rate of both thermal and gas-phase oxidative dehydrogenation reactions of ethane to ethylene as temperature increases.[32] The increase in the $CH_4/O_2$ ratio from 3 to 13 decreased the $C_2H_4/C_2H_6$ ratio to almost half at 750 °C, with a slight reduction observed at 600 °C (Figure 9). Increasing pressure from 1 to 10 bar decreased the ethylene selectivity from 25 to 9% at 800 °C (Figure 10b). The optimal condition for achieving the highest ethylene selectivity of 28.2% was found to be a $CH_4/O_2$ ratio of 9, temperature of 800 °C, and pressure of 1 bar.

The optimization results revealed that the temperature had the greatest impact on the selectivity of $C_2$, with a maximum selectivity of 65% achieved at 800 °C, a $CH_4/O_2$ ratio of 9, and a pressure of 1 bar (Table 6). However, increasing the temperature beyond this point may negatively affect catalyst stability. As shown in Figure 11a, an increase in temperature from 600 to 800 °C resulted in a significant increase in $C_2$


https://doi.org/10.1021/acsomega.3c02350
ACS Omega 2023, 8, 21223−21236

**Table 4. ANOVA Table of Ethane Selectivity**

| predictor | factor code | degree of freedom | sum of squares | *F* ratio | prob > *F* |
|---|---|---|---|---|---|
| $CH_4/O_2$ | *A* | 1 | 3071.8 | 187.51 | <.0001 |
| temperature | *B* | 1 | 1089.16 | 66.49 | <.0001 |
| pressure | *D* | 1 | 1161.8 | 70.92 | <.0001 |
| $CH_4/O_2$*temperature | *A***B* | 1 | 109.86 | 6.71 | 0.0110 |
| temperature*pressure | *B***D* | 1 | 1117.49 | 68.22 | <.0001 |
| source | degree of freedom | sum of squares | *F* ratio | mean square | |
| model | 5 | 14059.2 | 171.64 | 2811.84 | |
| error | 104 | 1703.71 | prob > *F* | 16.38 | |
| C. total | 109 | 15762.9 | <.0001 | | |

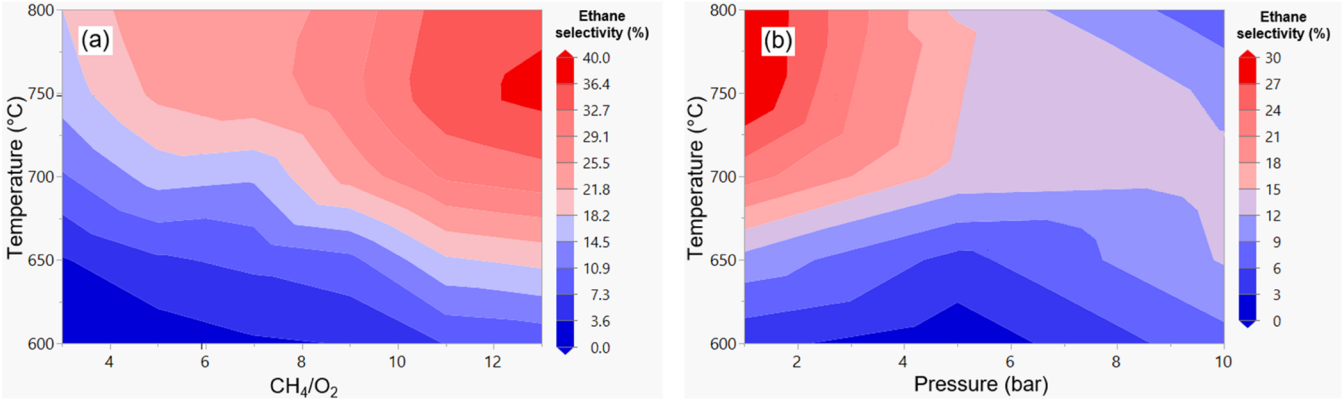


**Figure 8.** Ethane selectivity contour plots for (a) $CH_4/O_2$ versus temperature and (b) pressure versus temperature. Plots averaged all results based on the DoE calculation procedure.

**Table 5. ANOVA Table of Ethylene Selectivity**

| predictor | factor code | degree of freedom | sum of squares | *F* ratio | prob > *F* |
|---|---|---|---|---|---|
| $CH_4/O_2$ | *A* | 1 | 79.86 | 11.54 | 0.0010 |
| temperature | *B* | 1 | 1633.68 | 236.03 | <.0001 |
| pressure | *D* | 1 | 116.58 | 16.84 | <.0001 |
| temperature*pressure | *B***D* | 1 | 360.37 | 52.07 | <.0001 |
| source | degree of freedom | sum of squares | *F* ratio | mean square | |
| model | 4 | 8094.45 | 292.37 | 2023.61 | |
| error | 105 | 726.75 | prob > *F* | 6.92 | |
| C. total | 109 | 8821.2 | <.0001 | | |

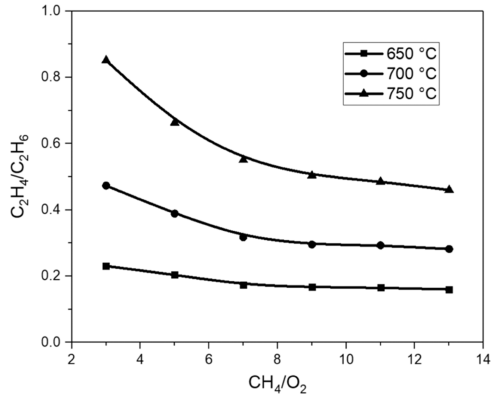


**Figure 9.** Ethylene to ethane ratio versus $CH_4/O_2$ ratio experimental results. 20 mg catalyst loading diluted with $SiO_2$, 70.7 kPa and $CH_4$, 101 kPa total pressure, $N_2$ as balance, and inlet volumetric flow rate 137 $cm^3$/min at 25 °C. The experimental error is within 5%. The lines represent B-spline fitting to the experimental data points.

selectivity from 6% to approximately 60% at a $CH_4/O_2$ ratio of 13. The temperature dependence of methane to $C_2$ conversion has been investigated in previous studies.[33,37] It was found that the conversion of methane to $C_2$ reactions becomes more favorable at higher temperatures. An increase in temperature was needed to overcome the $C_2$ activation energy. The exact value of the activation energy can vary depending on the catalyst used. Further experiments are necessary to ascertain the activation energy values accurately. The increase in pressure from 1 to 10 bar decreased the $C_2$ selectivity from 60 to 16% at 800 °C (Figure 11b). This effect can be explained by the fact that reaction R5, which is the primary pathway for $C_2$ generation, is a pressure-dependent reaction, as reported in the AramcoMech3.0 mechanism.[40] Furthermore, ANOVA statistical results showed that the quadratic and linear terms of the temperature had significant effects on $C_2$ selectivity, followed by the $CH_4/O_2$ ratio (Table 6). Increasing the $CH_4/O_2$ ratio from 3 to 13 increased the $C_2$ selectivity from 40% to more than 60% at 800 °C (Figure 11a). At $CH_4/O_2$ ratios below 7, part of the produced $C_2$ and other hydrocarbons could be further oxidized to $CO_x$ via reaction R11 (Figure 4).


https://doi.org/10.1021/acsomega.3c02350
ACS Omega 2023, 8, 21223−21236

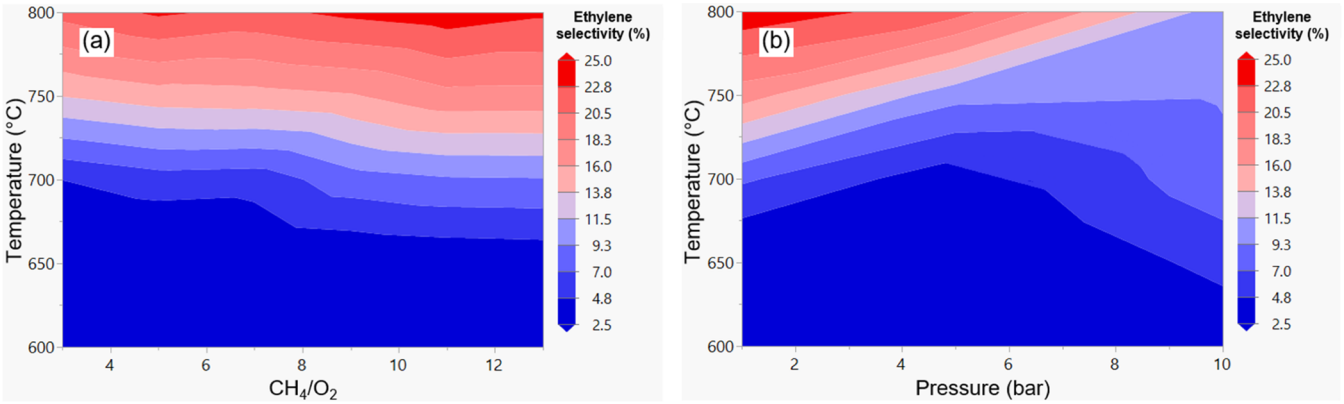


**Figure 10.** Ethylene selectivity contour plots for (a) $CH_4/O_2$ versus temperature and (b) pressure versus temperature. Plots averaged all results based on the DoE calculation procedure.

**Table 6. ANOVA Table of Ethane and Ethylene ($C_2$) Selectivity**

| predictor | factor code | degree of freedom | sum of squares | *F* ratio | prob > *F* |
|---|---|---|---|---|---|
| $CH_4/O_2$ | *A* | 1 | 4142.26 | 163.03 | <.0001 |
| temperature | *B* | 1 | 5390.67 | 212.17 | <.0001 |
| pressure | *D* | 1 | 2014.42 | 79.28 | <.0001 |
| $CH_4/O_2$*temperature | *A***B* | 1 | 153.7 | 6.05 | 0.0156 |
| temperature*pressure | *B***D* | 1 | 2747.04 | 108.12 | <.0001 |
| source | degree of freedom | sum of squares | *F* ratio | mean square | |
| model | 5 | 41294.31 | 325.06 | 8258.86 | |
| error | 104 | 2642.37 | prob > *F* | 25.41 | |
| C. total | 109 | 43936.68 | <.0001 | | |

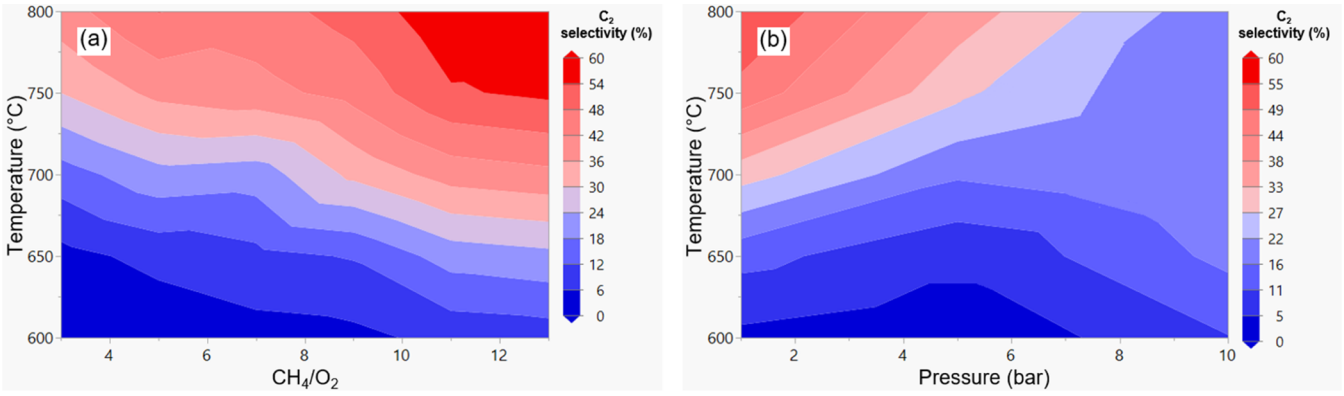


**Figure 11.** Ethane and ethylene ($C_2$) selectivity contour plots for (a) $CH_4/O_2$ versus temperature and (b) pressure versus temperature. Plots averaged all results based on the DoE calculation procedure.

Generally, high $CH_4/O_2$ ratios increase $C_2$ selectivity combined with a decrease in conversion. This decrease in conversion is a drawback and is attributed to the poor economics of the OCM.

**3.3. Carbon Monoxide and Carbon Dioxide ($CO_x$) Selectivity.** The quadratic formula for carbon monoxide and carbon dioxide ($CO_x$) selectivity is provided in eq 5. The obtained $R^2$ value of 0.94 confirms that the formula adequately describes the $CO_x$ selectivity. The parity plot for the $CO_x$ selectivity is shown in Figure 12. The symmetric distribution of data points along the diagonal of the plot shows high analytical accuracy in the prediction.

$$\begin{aligned} CO_x \text{ selectivity } (\%) &= 75.95 - 10.46\frac{A-8}{5} - 16.88\frac{B-700}{100} \\ &+ 7.27\frac{D-5.5}{4.5} - 3\frac{A-8}{5}\frac{B-700}{100} \\ &+ 12.54\frac{B-700}{100}\frac{D-5.5}{4.5} \end{aligned} \quad (5)$$

The selectivity of carbon monoxide and carbon dioxide was primarily influenced by the temperature, with linear and quadratic terms being significant (refer to Table 7). $CO_x$ selectivity declined from 94% to less than 40% as the temperature increased from 600 to 800 °C at a $CH_4/O_2$ ratio of 13 (Figure 13a). The $CO_x$ species were mostly formed through gas-phase reactions R12−R20 (Figure 4), wherein



https://doi.org/10.1021/acsomega.3c02350
ACS Omega 2023, 8, 21223−21236

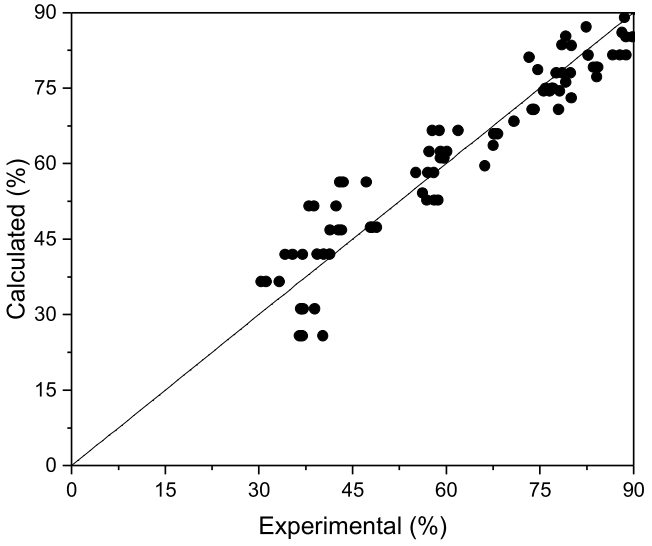


**Figure 12.** $CO_x$ selectivity parity plot for the experimental and predicted values.

methyl radicals were converted into methoxy species, followed by hydrogen removal steps.[39] Below 700 °C, the reactions were mainly driven thermodynamically to produce $CO_x$ through partial and complete oxidation reactions.[11] As stated, the $CO_x$ formation has a lower activation energy than ethane and thus requires less energy.[59] Upon increasing the pressure from 1 to 10 bar, the $CO_x$ formation was promoted, and its selectivity was increased from 40 to 80% at 800 °C (Figure 13b). The conversion of $CH_3O^*$ to $CH_2O$ via reaction R13 is highly pressure-dependent and plays a key role in controlling the formation of $CO_x$ via the methoxy species pathway.

Similar to previous responses, the $CH_4/O_2$ ratio was also a significant factor affecting the $CO_x$ selectivity, with a P-value of less than 5% (Table 7). Oxygen availability was a critical factor for converting methane to $CO_x$ via the complete oxidation of hydrocarbons. Reactions R1, R14, and R18, which, respectively, convert $CH_4$ to $CH_3$, $CH_3O$ to $CH_2O$, and HCO to CO, necessitate the presence of oxygen for their occurrence. Additionally, an alternative pathway that was observed involves the surface oxidation of ethylene, which can decrease the selectivity of $C_2$ through reaction R11.[39] As oxygen consumption reaches 100% conversion at temperatures above 750 °C, the first part of the reactor operates in an oxidative condition, while the remaining operates in a nonoxidative condition. To reduce the expenses of $CO_x$ separation and catalyst fouling caused by carbon deposition, it is recommended to operate at higher $CH_4/O_2$ ratios.[28,60] As the oxygen concentration decreased from a $CH_4/O_2$ ratio of 3 to 13, $CO_x$ formation decreased from 55% to less than 40% at 800 °C (Figure 13a). $CO_x$ formation generally decreased by increasing both the $CH_4/O_2$ ratio and temperature. This observation was in-line with the literature.[33,35,36] The minimum $CO_x$ selectivity obtained was 30.4% at 800 °C, a $CH_4/O_2$ ratio of 9, and a pressure of 1 bar.

**3.4. Ethane and Ethylene ($C_2$) Yield.** The empirical mathematical model for ethane and ethylene yield is provided in eq 6. The obtained $R^2$ value of 0.94 implies that the model can reproduce most of the variations in the response. The parity plot for the $C_2$ yield is shown in Figure 14, demonstrating a high degree of precision in the predictive analysis.

$$C_2\ \text{yield}\ (\%) = 3.22 - 0.46\frac{A-8}{5} + 2.73\frac{B-700}{100} - 1.28\frac{D-5.5}{4.5} - 1.23\frac{A-8}{5}\frac{B-700}{100} - 2.34\frac{B-700}{100}\frac{D-5.5}{4.5} \quad (6)$$

The efficiency of the OCM process is typically evaluated by measuring the yield of $C_2$, which is a critical metric for scalability. Our investigation revealed that the temperature has the most significant influence on the $C_2$ yield, followed by pressure, with a *P*-value lower than 5% (Table 8). As the temperature increased from 650 to 800 °C at a $CH_4/O_2$ ratio of 3, the $C_2$ yield increased from 1 to 12.2% (Figure 15a). However, the $C_2$ yield was restricted due to complete oxidation reactions that occur in both the gas phase and the catalyst surface. The maximum $C_2$ yield obtained in this study was 12.2% at 800 °C, a $CH_4/O_2$ ratio of 3, and a pressure of 1 bar. The obtained $C_2$ yield is comparable with a previous literature using a $La_2O_3/CeO_2$ catalyst.[11] The $C_2$ yield decreased from 12 to 2.5% when the pressure was increased from 1 to 10 bar at 800 °C (Figure 15b). Due to the exothermic nature of the OCM reaction, variations in the $CH_4/O_2$ ratio led to changes in the reaction temperature, which in turn affected the conversion and selectivity properties. Thus, the $CH_4/O_2$ ratio was found to be a sensitive variable for the $C_2$ yield (Table 8). The increase in oxygen concentration enhanced the formation rate of methyl radicals, followed by $C_2$ generation.[33,61] However, it should be noted that high oxygen concentrations inevitably lead to the production of $CO_x$.

## 4. CONCLUSIONS

One of the approaches to improve the OCM process involves investigating the effects of process variables and identifying the

**Table 7. ANOVA Table of Carbon Monoxide and Carbon Dioxide ($CO_x$) Selectivity**

| predictor | factor code | degree of freedom | sum of squares | *F* ratio | prob > *F* |
|---|---|---|---|---|---|
| $CH_4/O_2$ | *A* | 1 | 4685.93 | 151.44 | <.0001 |
| temperature | *B* | 1 | 6308.01 | 203.86 | <.0001 |
| pressure | *D* | 1 | 2128.05 | 68.77 | <.0001 |
| $CH_4/O_2$*temperature | *A***B* | 1 | 193.28 | 6.25 | 0.0140 |
| temperature*pressure | *B***D* | 1 | 3172.19 | 102.52 | <.0001 |
| source | degree of freedom | sum of squares | *F* ratio | mean square | |
| model | 5 | 47725.16 | 308.47 | 9545.03 | |
| error | 104 | 3218.12 | prob > *F* | 30.94 | |
| C. total | 109 | 50943.28 | <.0001 | | |



https://doi.org/10.1021/acsomega.3c02350
ACS Omega 2023, 8, 21223−21236

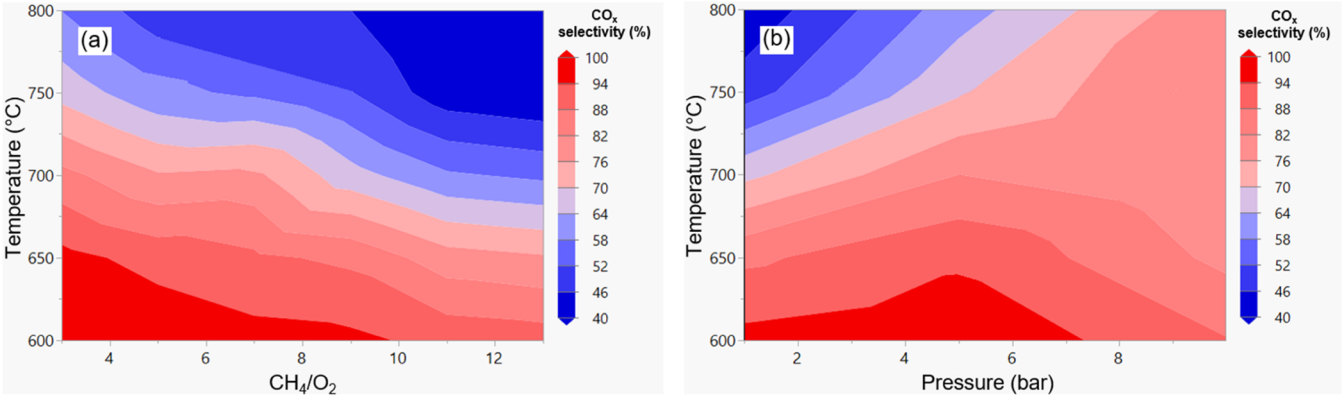


**Figure 13.** Carbon monoxide and carbon dioxide ($CO_x$) selectivity contour plots for (a) $CH_4/O_2$ versus temperature and (b) pressure versus temperature. Plots averaged all results based on the DoE calculation procedure.

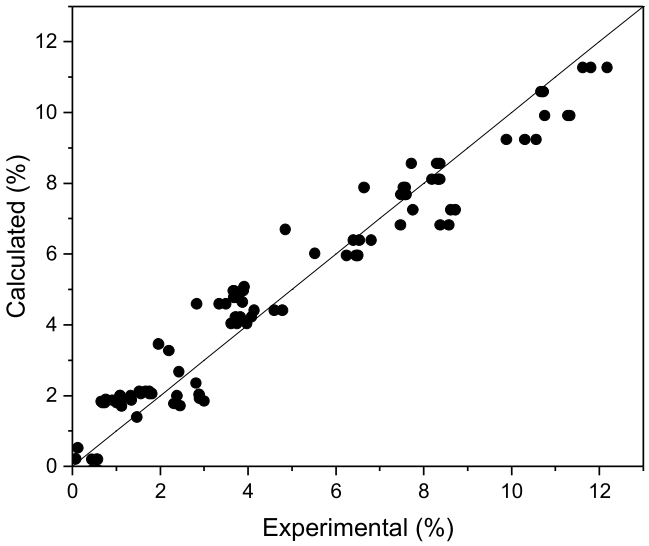


**Figure 14.** $C_2$ yield parity plot for the experimental and predicted values.

optimum process parameters to maximize the $C_2$ yield. Four process variables, temperature, $CH_4/O_2$ ratio, pressure, and catalyst loading, were examined at a wide range of operating conditions to comprehend the complex homogeneous–heterogeneous chemistry involved in OCM. The DoE method was implemented with ANOVA to achieve the maximum methane conversion toward $C_2$ and minimize $CO_x$ using a $La_2O_3$-based catalyst. The design of experiments with systematic optimization presented an efficient practical method for analyzing the process performance. The derived quadratic equations with $R^2$ greater than 0.9 provided satisfactory analytical predictions of the conversion and selectivity properties. This finding is important as it suggests that the quadratic equations have practical applicability and can guide future research to optimize different catalyst systems. The process performance was found to be primarily influenced by the $CH_4/O_2$ ratio and temperature. The linear variable had the greatest impact, followed by the quadratic terms. The increase in oxygen concentration was observed to increase methane conversion and $CO_x$ selectivity while decreasing the selectivity of $C_2$, which is a drawback from an economic perspective. Conversely, the temperature increased methane conversion, $C_2$ selectivity, and decreased $CO_x$ selectivity. The increase in pressure decreased the selectivity and yield of $C_2$ while promoting undesired total oxidation reactions to form $CO_x$. The optimum conversion of 18% and $C_2$ selectivity of 61% were achieved at 800 °C and a $CH_4/O_2$ ratio of 7. The maximum $C_2$ yield obtained was 12.2% at 800 °C, a $CH_4/O_2$ ratio of 3, and a pressure of 1 bar. Owing to the large experimental data set collected, this study provides a better prediction of the products, which can contribute directly to the development of the OCM reactor size and downstream processes, further including their economic evaluation. The ROP analysis was employed to elucidate the responses observed in the light of reaction pathways and to provide insights for the development of future catalysts. The results indicated that oxygen was rapidly consumed, reaching 100% conversion leading to the saturation of conversion and product selectivities. Therefore, a multi-oxygen injector concept, like a membrane reactor, would be attractive.[2,11,62] A fixed-bed reactor with an oxygen-permeable membrane, such as an ion transport membrane, which allows oxygen to permeate along

**Table 8. ANOVA Table of Ethane and Ethylene ($C_2$) Yield**

| predictor | factor code | degree of freedom | sum of squares | *F* ratio | prob > *F* |
|---|---|---|---|---|---|
| $CH_4/O_2$ | *A* | 1 | 9.07 | 11.83 | 0.0008 |
| temperature | *B* | 1 | 165.54 | 215.98 | <.0001 |
| pressure | *D* | 1 | 66.05 | 86.18 | <.0001 |
| $CH_4/O_2$*temperature | *A***B* | 1 | 32.57 | 42.49 | <.0001 |
| temperature*pressure | *B***D* | 1 | 110.27 | 143.87 | <.0001 |
| source | degree of freedom | sum of squares | *F* ratio | mean square | |
| model | 5 | 1311.38 | 342.19 | 262.28 | |
| error | 104 | 79.71 | prob > *F* | 0.77 | |
| C. total | 109 | 1391.09 | <.0001 | | |



https://doi.org/10.1021/acsomega.3c02350
ACS Omega 2023, 8, 21223−21236

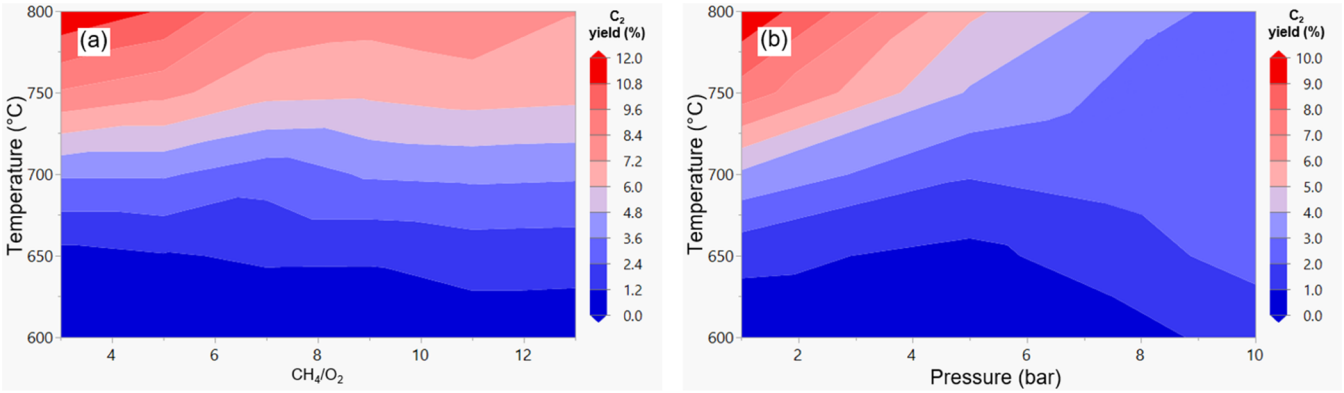


**Figure 15.** Ethane and ethylene ($C_2$) yield contour plots for (a) $CH_4/O_2$ versus temperature and (b) pressure versus temperature. Plots averaged all results based on the DoE calculation procedure.

the length of the catalyst bed is desirable to maximize the methane conversion and selectivity of $C_2$. The oxygen and methane are not premixed before entering the reaction zone. Oxygen concentration level within the reaction zone is important to promote methane activation and decrease carbon formation and deposition.

## AUTHOR INFORMATION


### Corresponding Authors

**Sultan Alturkistani** − *Physical Sciences and Engineering Division, King Abdullah University of Science and Technology (KAUST), CCRC, Jeddah 23955-6900, Saudi Arabia; Physical Sciences and Engineering Division, King Abdullah University of Science and Technology (KAUST), KAUST Catalysis Center, Jeddah 23955-6900, Saudi Arabia;* Phone: +966 568 232 346; Email: sultan.alturkistani@kaust.edu.sa

**Ribhu Gautam** − *Physical Sciences and Engineering Division, King Abdullah University of Science and Technology (KAUST), CCRC, Jeddah 23955-6900, Saudi Arabia;* orcid.org/0000-0002-5567-7778; Email: ribhu.gautam@kaust.edu.sa

### Authors

**Haoyi Wang** − *Physical Sciences and Engineering Division, King Abdullah University of Science and Technology (KAUST), CCRC, Jeddah 23955-6900, Saudi Arabia; Physical Sciences and Engineering Division, King Abdullah University of Science and Technology (KAUST), KAUST Catalysis Center, Jeddah 23955-6900, Saudi Arabia;* orcid.org/0000-0002-6865-0646

**S. Mani Sarathy** − *Physical Sciences and Engineering Division, King Abdullah University of Science and Technology (KAUST), CCRC, Jeddah 23955-6900, Saudi Arabia;* orcid.org/0000-0002-3975-6206

Complete contact information is available at: https://pubs.acs.org/10.1021/acsomega.3c02350



### Funding

The work presented in this paper was funded by King Abdullah University of Science and Technology (KAUST).


### Notes

The authors declare no competing financial interest.


## ACKNOWLEDGMENTS

All experiments were performed in the King Abdullah University of Science and Technology (KAUST), Saudi Arabia. The author gratefully acknowledges SABIC and KAUST for funding this project.


## REFERENCES


(1) Kee, R. J.; Karakaya, C.; Zhu, H. Process intensification in the catalytic conversion of natural gas to fuels and chemicals. *Proc. Combust. Inst.* **2017**, *36*, 51−76.

(2) Karakaya, C.; Kee, R. J. Progress in the direct catalytic conversion of methane to fuels and chemicals. *Prog. Energy Combust. Sci.* **2016**, *55*, 60−97.

(3) Keller, G.; Bhasin, M. Synthesis of ethylene via oxidative coupling of methane: I. Determination of active catalysts. *J. Catal.* **1982**, *73*, 9−19.

(4) Arndt, S.; Simon, U.; Heitz, S.; Berthold, A.; Beck, B.; Görke, O.; Epping, J.-D.; Otremba, T.; Aksu, Y.; Irran, E.; et al. Li-doped MgO from different preparative routes for the oxidative coupling of methane. *Top. Catal.* **2011**, *54*, 1266−1285.

(5) Martin, G.; Mirodatos, C. Surface chemistry in the oxidative coupling of methane. *Fuel Process. Technol.* **1995**, *42*, 179−215.

(6) McCarty, J. G. Mechanism of Cooxidative Methane Dimerization Catalysis: Kinetic and Thermodynamic Aspects. In *Methane Conversion by Oxidative Processes*; Springer, 1992; pp 320−350.

(7) Nelson, P. F.; Lukey, C. A.; Cant, N. W. Isotopic evidence for direct methyl coupling and ethane to ethylene conversion during partial oxidation of methane over lithium/magnesium oxide. *J. Phys. Chem. A* **1988**, *92*, 6176−6179.

(8) Su, Y.; Ying, J. Y.; Green, W. H., Jr Upper bound on the yield for oxidative coupling of methane. *J. Catal.* **2003**, *218*, 321−333.

(9) Lunsford, J. H. Catalytic conversion of methane to more useful chemicals and fuels: a challenge for the 21st century. *Catal. Today* **2000**, *63*, 165−174.

(10) Reyes, S. C.; Iglesia, E.; Kelkar, C. Kinetic-transport models of bimodal reaction sequences—I. Homogeneous and heterogeneous pathways in oxidative coupling of methane. *Chem. Eng. Sci.* **1993**, *48*, 2643−2661.

(11) Karakaya, C.; Zhu, H.; Zohour, B.; Senkan, S.; Kee, R. J. Detailed reaction mechanisms for the oxidative coupling of methane over La2O3/CeO2 nanofiber fabric catalysts. *ChemCatChem* **2017**, *9*, 4538−4551.

(12) Karakaya, C.; Zhu, H.; Loebick, C.; Weissman, J. G.; Kee, R. J. A detailed reaction mechanism for oxidative coupling of methane over Mn/Na2WO4/SiO2 catalyst for non-isothermal conditions. *Catal. Today* **2018**, *312*, 10−22.

(13) Akin, F.; Lin, Y. Controlled oxidative coupling of methane by ionic conducting ceramic membrane. *Catal. Lett.* **2002**, *78*, 239−242.

(14) Deboy, J. M.; Hicks, R. F. Kinetics of the oxidative coupling of methane over 1 wt% SrLa2O3. *J. Catal.* **1988**, *113*, 517−524.
(15) Elkins, T. W.; Hagelin-Weaver, H. E. Characterization of Mn−Na 2 WO 4/SiO 2 and Mn−Na 2 WO 4/MgO catalysts for the oxidative coupling of methane. *Appl. Catal., A* **2015**, *497*, 96−106.
(16) Feng, Y.; Niiranen, J.; Gutman, D. Kinetic studies of the catalytic oxidation of methane. 1. Methyl radical production on 1% strontium/dilanthanum trioxide. *J. Phys. Chem. A* **1991**, *95*, 6558−6563.
(17) Hiyoshi, N.; Ikeda, T. Oxidative coupling of methane over alkali chloride−Mn−Na2WO4/SiO2 catalysts: Promoting effect of molten alkali chloride. *Fuel Process. Technol.* **2015**, *133*, 29−34.
(18) Koirala, R.; Büchel, R.; Pratsinis, S. E.; Baiker, A. Oxidative coupling of methane on flame-made Mn-Na2WO4/SiO2: Influence of catalyst composition and reaction conditions. *Appl. Catal., A* **2014**, *484*, 97−107.
(19) Liu, H.; Wang, X.; Yang, D.; Gao, R.; Wang, Z.; Yang, J. Scale up and stability test for oxidative coupling of methane over Na2WO4-Mn/SiO2 catalyst in a 200 ml fixed-bed reactor. *J. Nat. Gas Chem.* **2008**, *17*, 59−63.
(20) Taylor, R. P.; Schrader, G. L. Lanthanum catalysts for methane oxidative coupling: a comparison of the reactivity of phases. *Ind. Eng. Chem. Res.* **1991**, *30*, 1016−1023.
(21) Xu, M.; Lunsford, J. H. Effect of temperature on methyl radical generation over Sr/La 2 O 3 catalysts. *Catal. Lett.* **1991**, *11*, 295−300.
(22) Fang, X.; Li, S.; Lin, J.; Chu, Y. Oxidative Coupling of Methane on W-Mn Catalysts. *J. Mol. Catal.* **1992**, *6*, 427−433.
(23) Ito, T.; Wang, J.; Lin, C. H.; Lunsford, J. H. Oxidative dimerization of methane over a lithium-promoted magnesium oxide catalyst. *J. Am. Chem. Soc.* **1985**, *107*, 5062−5068.
(24) Myrach, P.; Nilius, N.; Levchenko, S. V.; Gonchar, A.; Risse, T.; Dinse, K. P.; Boatner, L. A.; Frandsen, W.; Horn, R.; Freund, H. J.; et al. Temperature-Dependent Morphology, Magnetic and Optical Properties of Li-Doped MgO. *ChemCatChem* **2010**, *2*, 854−862.
(25) Zavyalova, U.; Holena, M.; Schlögl, R.; Baerns, M. Statistical analysis of past catalytic data on oxidative methane coupling for new insights into the composition of high-performance catalysts. *ChemCatChem* **2011**, *3*, 1935−1947.
(26) Schammel, W. P.; Wolfenbarger, J.; Ajinkya, M.; McCarty, J.; Cizeron, J. M.; Weinberger, S.; Edwards, J. D.; Sheridan, D.; Scher, E. C.; McCormick, J. Oxidative coupling of methane systems and methods *Google Patents* 2016.
(27) Choudhary, V. R.; Mulla, S. A.; Rane, V. H. Surface basicity and acidity of alkaline earth-promoted La2O3 catalysts and their performance in oxidative coupling of methane. *J. Chem. Technol. Biotechnol.* **1998**, *72*, 125−130.
(28) Noon, D.; Seubsai, A.; Senkan, S. Oxidative coupling of methane by nanofiber catalysts. *ChemCatChem* **2013**, *5*, 146−149.
(29) Marafee, A.; Liu, C.; Xu, G.; Mallinson, R.; Lobban, L. An experimental study on the oxidative coupling of methane in a direct current corona discharge reactor over Sr/La2O3 catalyst. *Ind. Eng. Chem. Res.* **1997**, *36*, 632−637.
(30) Petrov, R.; Reshetnikov, S.; Ivanova, Y.; Isupova, L. Study of the kinetic regularities of the oxidative methane coupling over Sr-La2O3 material. *J. Phys.: Conf. Ser.* **2019**, *1145*, No. 012023.
(31) Sollier, B. M.; Gómez, L. E.; Boix, A. V.; Miró, E. E. Oxidative coupling of methane on cordierite monoliths coated with Sr/La2O3 catalysts. Influence of honeycomb structure and catalyst-cordierite chemical interactions on the catalytic behavior. *Appl. Catal., A* **2018**, *550*, 113−121.
(32) Choudhary, V. R.; Uphade, B. S.; Mulla, S. A. Oxidative coupling of methane over a Sr-promoted La2O3 catalyst supported on a low surface area porous catalyst carrier. *Ind. Eng. Chem. Res.* **1997**, *36*, 3594−3601.
(33) Amin, N. A. S.; Pheng, S. E. Influence of process variables and optimization of ethylene yield in oxidative coupling of methane over Li/MgO catalyst. *Chem. Eng. J.* **2006**, *116*, 187−195.
(34) Eppinger, T.; Wehinger, G.; Kraume, M. Parameter optimization for the oxidative coupling of methane in a fixed bed reactor by combination of response surface methodology and computational fluid dynamics. *Chem. Eng. Res. Des.* **2014**, *92*, 1693−1703.
(35) Kundu, P. K.; Zhang, Y.; Ray, A. K. Multi-objective optimization of simulated countercurrent moving bed chromatographic reactor for oxidative coupling of methane. *Chem. Eng. Sci.* **2009**, *64*, 4137−4149.
(36) Quddus, M. R.; Zhang, Y.; Ray, A. K. Multi-objective optimization in solid oxide fuel cell for oxidative coupling of methane. *Chem. Eng. J.* **2010**, *165*, 639−648.
(37) Thien, C. Y.; Mohamed, A. R.; Bhatia, S. Process optimization of oxidative coupling of methane for ethylene production using response surface methodology. *J. Chem. Technol. Biotechnol.* **2007**, *82*, 81−91.
(38) Thanasiriruk, M.; Saychoo, P.; Khajonvittayakul, C.; Tongnan, V.; Hartley, U. W.; Laosiripojana, N. Optimizing Operating Conditions for Oxidative Coupling Methane (OCM) in the Presence of NaCl-MnOx/SiO2. *Appl. Sci. Eng. Prog.* **2021**, *14*, 477−488.
(39) Alturkistani, S.; Wang, H.; Yalamanchi, K.; Gautam, R.; Sarathy, M. In *High-Throughput Experiments and Kinetic Modeling of Oxidative Coupling of Methane, OCM Over $La_2O_3/CeO_2$ Catalyst*, ADIPEC; OnePetro, 2022.
(40) Zhou, C.-W.; Li, Y.; Burke, U.; Banyon, C.; Somers, K. P.; Ding, S.; Khan, S.; Hargis, J. W.; Sikes, T.; Mathieu, O.; et al. An experimental and chemical kinetic modeling study of 1, 3-butadiene combustion: Ignition delay time and laminar flame speed measurements. *Combust. Flame* **2018**, *197*, 423−438.
(41) Brinker, C. J.; Scherer, G. W. *Sol-Gel Science: the Physics and Chemistry of Sol-Gel Processing*; Academic Press, 2013.
(42) Klein, L. C. Sol-gel processing of silicates. *Annu. Rev. Mater. Sci.* **1985**, *15*, 227−248.
(43) Livage, J.; Henry, M.; Sanchez, C. Sol-gel chemistry of transition metal oxides. *Prog. Solid State Chem.* **1988**, *18*, 259−341.
(44) McMurdie, H. F.; Morris, M. C.; Evans, E. H.; Paretzkin, B.; Wong-Ng, W.; Ettlinger, L.; Hubbard, C. R. Standard X-ray diffraction powder patterns from the JCPDS research associateship. *Powder Diffr.* **1986**, *1*, 64−77.
(45) McMurdie, H.; Morris, M.; Evans, E.; Paretzkin, B.; Wong-Ng, W.; Hubbard, C. Methods of Producing Standard X-Ray Diffraction Powder Patterns. *Powder Diffr.* **1986**, *1*, 40−43.
(46) Khidirov, I.; Om, V. Localization of hydrogen atoms in rare earth metal trihydroxides R (OH) 3. *Phys. Status Solidi (a)* **1993**, *140*, K59−K62.
(47) Tang, C. C.; Bando, Y.; Liu, B.; Golberg, D. Cerium oxide nanotubes prepared from cerium hydroxide nanotubes. *Adv. Mater.* **2005**, *17* (24), 3005−3009.
(48) Hanawalt, J.; Rinn, H.; Frevel, L. Chemical analysis by X-ray diffraction. *Ind. Eng. Chem., Anal. Ed.* **1938**, *10*, 457−512.
(49) Hamm, C. M.; Alff, L.; Albert, B. Synthesis of microcrystalline Ce2O3 and formation of solid solutions between cerium and lanthanum oxides. *Z. Anorg. Allg. Chem.* **2014**, *640*, 1050−1053.
(50) Attfield, J. P.; Ferey, G. Structure determinations of La2O2CO3-II and the unusual disordered phase La2O2. 52 (CO3) 0.74 Li0. 52 using powder diffraction. *J. Solid State Chem.* **1989**, *82*, 132−138.
(51) Levan, T.; Che, M.; Tatibouet, J.; Kermarec, M. Infrared study of the formation and stability of La2O2CO3 during the oxidative coupling of methane on La2O3. *J. Catal.* **1993**, *142*, 18−26.
(52) Montgomery, D. C. *Design and Analysis of Experiments*; John wiley & sons, 2017.
(53) Jašo, S.; Godini, H.; Arellano-Garcia, H.; Omidkhah, M.; Wozny, G. Analysis of attainable reactor performance for the oxidative methane coupling process. *Chem. Eng. Sci.* **2010**, *65*, 6341−6352.
(54) Driscoll, D. J.; Martir, W.; Wang, J. X.; Lunsford, J. H. Formation of gas-phase methyl radicals over magnesium oxide. *J. Am. Chem. Soc.* **1985**, *107*, 58−63.
(55) Chen, Q.; Couwenberg, P.; Marin, G. Effect of pressure on the oxidative coupling of methane in the absence of catalyst. *AIChE J.* **1994**, *40*, 521−535.


https://doi.org/10.1021/acsomega.3c02350
*ACS Omega* 2023, 8, 21223−21236

(56) Warnatz, J. Rate Coefficients in the C/H/O System In *Combustion Chemistry*; Springer, 1984; pp 197−360.
(57) Liu, Z.; Li, J. P. H.; Vovk, E.; Zhu, Y.; Li, S.; Wang, S.; van Bavel, A. P.; Yang, Y. Online kinetics study of oxidative coupling of methane over La2O3 for methane activation: what is behind the distinguished light-off temperatures? *ACS Catal.* **2018**, *8*, 11761−11772.
(58) Rane, V. H.; Chaudhari, S. T.; Choudhary, V. R. Comparison of the surface and catalytic properties of rare earth-promoted CaO catalysts in the oxidative coupling of methane. *J. Chem. Technol. Biotechnol.* **2006**, *81*, 208−215.
(59) Mleczko, L.; Baerns, M. Catalytic oxidative coupling of methane—reaction engineering aspects and process schemes. *Fuel Process. Technol.* **1995**, *42*, 217−248.
(60) Zohour, B.; Noon, D.; Senkan, S. Spatial Concentration and Temperature Profiles in Dual-Packed-Bed Catalytic Reactors: Oxidative Coupling of Methane. *ChemCatChem* **2014**, *6*, 2815−2820.
(61) Nibbelke, R.; Scheerova, J.; De Croon, M.; Marin, G. The oxidative coupling of methane over MgO-based catalysts: A steady-state isotope transient kinetic analysis. *J. Catal.* **1995**, *156*, 106−119.
(62) Lu, Y.; Dixon, A. G.; Moser, W. R.; Ma, Y. H. Analysis and optimization of cross-flow reactors for oxidative coupling of methane. *Ind. Eng. Chem. Res.* **1997**, *36*, 559−567.



https://doi.org/10.1021/acsomega.3c02350
*ACS Omega* 2023, 8, 21223−21236